doi: 10.1038/nature07095

SUPPLEMENTARY INFORMATION

Experimental determination of frequency

In-situ rotation of the cantilever and sample (both placed on a rotator) is performed to minimise cantilever deflection due to vortex pinning and de Haas-van Alphen (dHvA) oscillation contributions (see Fig. 1 of main text), thereby reducing the possibility of torque interaction effects. Since the frequency of the oscillations varies as $F \approx F_0/\cos\theta$, where θ is the angle between **H** and the crystalline c-axis[10], the above procedure enables the minimal Fermi surface cross-sections to be determined. In order to overcome as far as possible limitations of the narrow field range over which oscillations are observed at 30 mK, we extract a value of the α frequency from higher temperature data. A frequency $F_\alpha \approx 500 \pm 20$ T is obtained from averaging several field sweeps at 1.5 K and extracting oscillations observed over a wider interval in magnetic field ($32 < \mu_0 H < 45$ T) due to a reduction in contribution from vortex pinning at these high temperatures (see Fig. S1). This estimate is somewhat lower than the frequency $F_\alpha \approx 520 \pm 30$ T obtained from fits in the field interval $38 < \mu_0 H < 45$ T to field sweeps at 30 mK in this work, and that obtained in ref. 7 ($F_\alpha \approx 530 \pm 20$ T) and ref. 10 ($F_\alpha \approx 540 \pm 4$ T). This difference could possibly be explained by factors such as a difference in field orientation, a magnetic field-dependence of F_α, or the presence of a weak additional frequency.

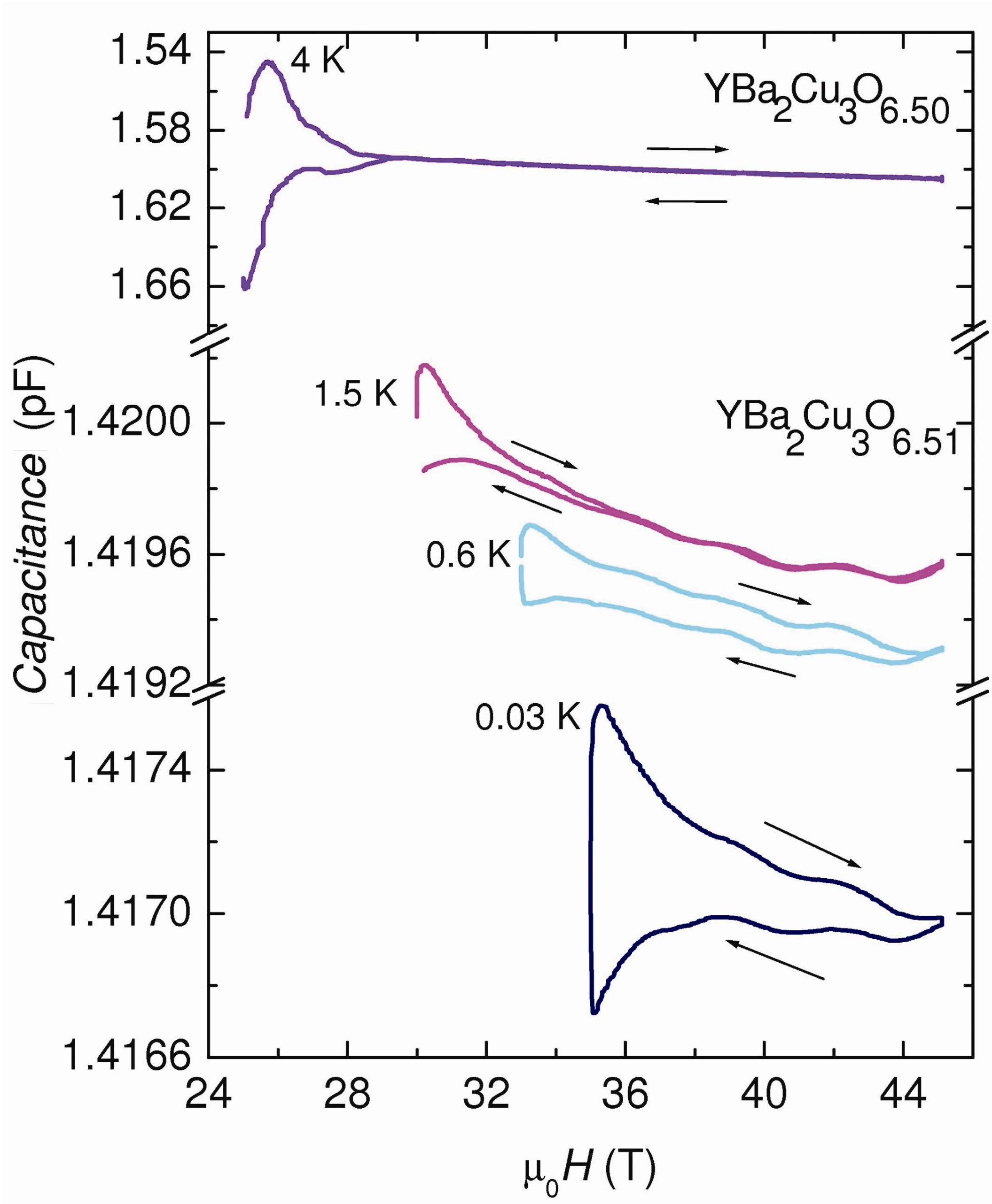

Fig. S1. Hysteresis loops in the capacitance, Measured capacitance at different temperatures (the zero magnetic field value = 1.4358pF). The cantilever has been optimised for maximum sensitivity within its linear response regime in the high magnetic field regime where measurements have been made on $YBa_2Cu_3O_{6.51}$. Also shown is a similar measurement of $YBa_2Cu_3O_{6.50}$ at 4 K.

Harmonic Analysis

The proximity of the ratio F_β/F_α to 3 raises a potential concern as to whether the β frequency corresponds to a harmonic of the α frequency rather than a separate Fermi surface section. The effective mass ratio of $m^*_\beta/m^*_\alpha \approx 2$ implies that such a harmonic would need to originate from a non-linearity in the dHvA oscillations due, for example, to oscillations of the chemical potential[31] or torque interaction effects rather than the Lifshitz-Kosevich theory[11]. To a first approximation, such non-linearities would introduce an additional sinusoidal factor inside the argument of the periodic term in the dHvA effect (i.e.) $\mathcal{A}_B/B = \mathcal{A}_0 \sin(2\pi F(1+k\sin(2\pi F/B+\phi))/B+\phi)\exp(-\zeta/B)$ [Refs. 11,31] where $|k| \sim (B/F)^2\exp(-\zeta/B) \sim 1.5\times10^{-4}$ and $|k| \sim \theta d\theta \sim 3\times10^{-7}$ (at fields ~ 41 T) for oscillations of the chemical potential and torque interaction respectively. The associated distortion of the signal would introduce additional harmonics that decay in amplitude with increasing harmonic index. Simulations indicate that the large value of ζ_α (Fig. 3b of the main manuscript) precludes oscillations of the chemical potential as a significant effect[33], while the small angular displacement $d\theta \approx 0°\,0'\,1''$ of the cantilever (corresponding to the dHvA oscillations) would lead to an imperceptibly small harmonic distortion of the dHvA signal. Further, the weak $2F_\alpha$ feature in the experimental Fourier transform (Fig. 2a) is not intermediate in amplitude between that of F_α and F_β, and therefore appears inconsistent with a non-linear dHvA effect signal. Rather, the relative phase of the $2F_\alpha$ harmonic (Fig. S2) is consistent with the two dimensional Lifshitz Kosevich expression[33], indicative of damping of the F_α chemical potential oscillations by a large charge reservoir, as would be provided by the heavier β pocket.

Fig. S2 shows measured oscillations at 30 mK from Fig. 2b as a function of $1/\mu_0H$ and the isolated β frequency component obtained on subtracting a sinusoidal fit to the α frequency oscillations plus a small contribution from 2α plus a residual fifth order polynomial. The β frequency oscillations shown over a reduced range in μ_0H in

Fig. 2c are extracted using such a procedure. Also shown by vertical lines in the figure are the maxima of the F_β and F_α oscillations and anticipated maxima of the $3F_\alpha$ harmonics of the alpha frequency. The $1/\mu_0H$-dependent separation between the F_β oscillation maxima and the locations where the $3F_\alpha$ oscillation maxima would occur suggests that F_β does not correspond to $3F_\alpha$.

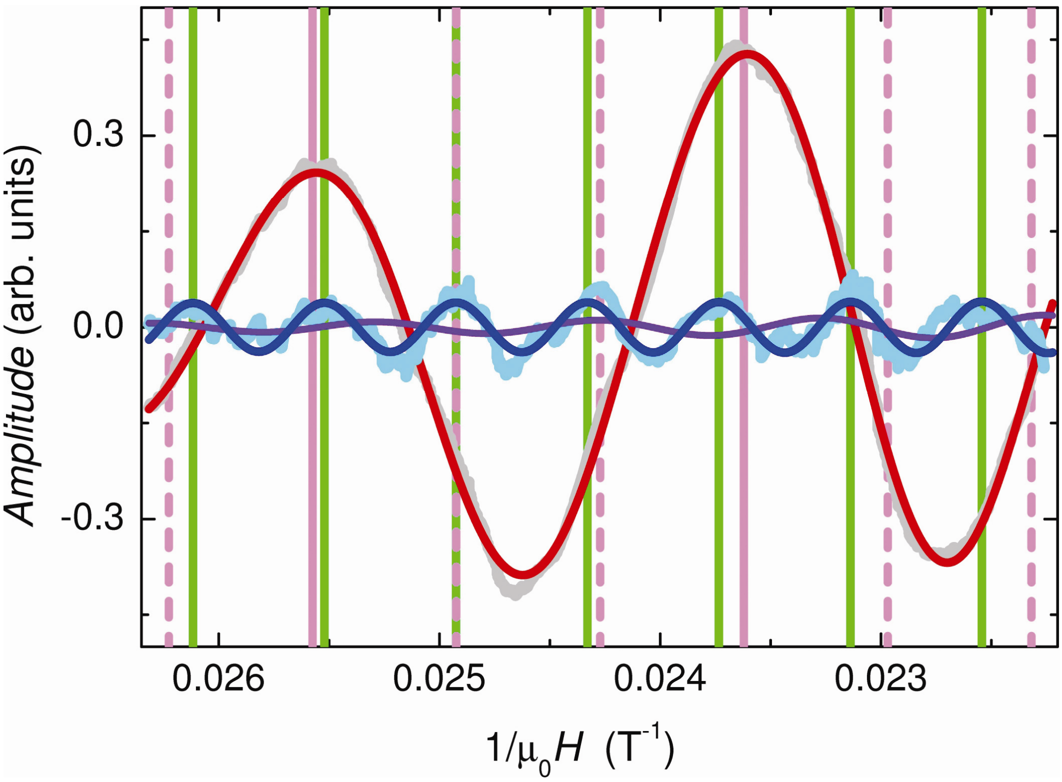

Fig. S2. Separation of the signal into α and β frequency components. The grey curve corresponds to the 30 mK data in Fig. 2b. The β component (shown in cyan, multiplied by a factor of two) is isolated by subtracting a sinusoidal fit to the **α** oscillations plus small contributions from a 2α component (shown in purple) and a 5th order polynomial term (sum shown in red – the oscillatory α component of this fit alone is shown in Fig. 3 of the main text). A sinusoidal fit to the β frequency oscillations is also shown for clarity (blue). Vertical purple and green lines are drawn to represent the fields at which respective maxima in the α and β frequency torque oscillations occur, with additional dotted magenta lines representing the anticipated maxima of the $3F_\alpha$ harmonic.

Magnetic quantum oscillations and the vortex state

Vortex pinning within the mixed state leads to magnetic hysteresis over an extensive range of magnetic field between rising and falling magnetic fields, up to the irreversibility field H_{irr}. The torque of $YBa_2Cu_3O_{6.51}$ is observed to be hysteretic over the entire range of magnetic field at base temperature ($T \approx 30$ mK), indicating that $\mu_0 H_{irr} > 45$ T (see Fig. S1). The change in field sweep direction at 45 T leads to an abrupt jump in the torque on reversing the polarity of the trapped flux. On increasing the temperature of the sample above 600 mK by applying heat to the dilution mixture in which the sample is in thermal contact, $\mu_0 H_{irr}$ is observed to fall below 45 T. The extracted H_{irr} versus T plot shown in Fig. S3 is similar to the flux lattice melting line measured on compositionally similar samples by Taylor and Maple[34]. Differences in sample composition between different groups likely account for a small shift between the curves. We find three different UBC crystals of varying size and shape to lie on a single curve in Fig. S3, further exhibiting a behaviour consistent with the universal Lindemann model[34]. The observation of hysteresis to magnetic fields of 45 T suggests that vortices are present throughout the experiment at the lowest temperatures[34], with the flux-lattice melting line playing the important role of a corroboratory in-situ temperature calibration.

The existence of dHvA oscillations within the vortex state is now confirmed in a wide variety of type II superconductors, key observations having been established in some early work[30]. The dHvA frequencies and effective masses are unchanged with respect to those in the normal state, but the quantum oscillations experience some additional damping, which is traditionally interpreted as an additional field-dependent scattering rate τ_s^{-1}. The effective scattering rate arises from the paired quasiparticles in Landau quantized states that constitute the Cooper pairs for $H_{c1} << H < H_{c2}$. The pair potential broadens the otherwise degenerate Landau levels, introducing an effective τ_s^{-1} that depends on the spatially averaged square of the superconducting order parameter Ψ (Ref 35). We use the expression determined by Yasui and Kita[36] to estimate a value for the scattering rate: $\tau_s^{-1} \approx \tilde{\Gamma}\frac{\Psi^2}{\hbar^2\omega_c}$ where $\tilde{\Gamma} \approx 0.125$ for *s*-wave superconductivity and $\omega_c = eB/m^*$. In the case of $YBa_2Cu_3O_{6.51}$, we estimate τ_s^{-1} at B = 38.5 T assuming that $2\Psi_0 = 3.52\ k_BT_c$ where $T_c \approx 57.5$ K, $\Psi^2 = \Psi_0^2(1 - H/H_{c2})$ and $\mu_0H_{c2} \approx 60$ T (see Fig. S3). A value of $\tau_s^{-1} \geq 2.2 \times 10^{12}$ s^{-1} is obtained for the α pocket, implying clearly observable oscillations.

Similar calculations yield a value of $\tau_s^{-1} \geq 4.4 \times 10^{12}$ s^{-1} for the β pocket., which would imply an oscillation amplitude ~400 times smaller in size than the α oscillations (since the argument of the exponential damping term scales with the square of m^*). Additional factors are, however, likely to affect the oscillation amplitudes, leading to the visibility of β oscillations in the experiment – for instance, the nodal form of the *d*-wave superconducting wavefunction is predicted to have an important effect[36]. In this case, Ψ is expected to be reduced[36] depending of the proximity of a given pocket to the node in the superconducting wavefunction in *k*-space. For an electron pocket situated near the antinode at (π,0), Ψ would be minimally reduced relative to that of the *s*-wave case. However, for a hole pocket situated near the node at (π/2,π/2), Ψ could be strongly reduced, perhaps explaining survival of the β frequency and its comparably weak field dependence deep within the vortex state. We note that it is likely that a modified theory for τ_s^{-1} needs to be developed to account for the competition between superconductivity and magnetism.

Were there to be no vortex state contribution to the scattering rate, a simple $\mathcal{A}_B/B = \mathcal{A}_0\sin(2\pi F/B+\phi)\exp(-\zeta/B)$ fit (shown in Fig. 3) would yield $\tau_\alpha^{-1} \sim 4.6 \pm 1.5 \times 10^{12}$ s^{-1} corresponding to the fit value of $\zeta_\alpha = 160 \pm 50$ T. Such a scattering rate would imply an electron mobility $\mu_\alpha = e\tau/m_\alpha^* = \pi/\zeta_\alpha \approx (2.0 \pm 0.5) \times 10^{-2}$ T^{-1}, and mean free path $l_\alpha = 170 \pm 50$ Å.

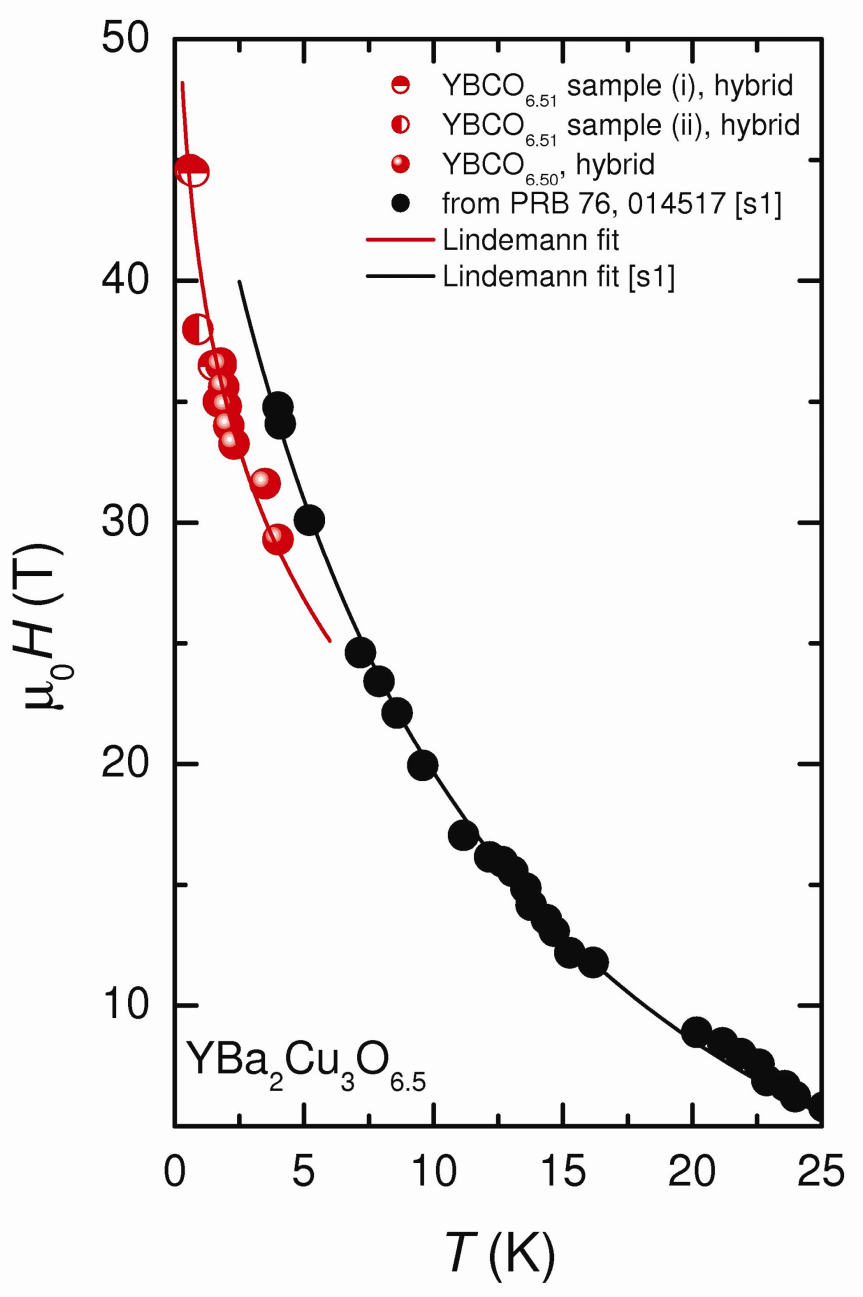

Fig. S3. The flux-lattice melting curve of $YBa_2Cu_3O_{6.5}$. Data are shown for three different samples (red) from measurements like those presented in Fig. S1. The points correspond to the field H_{irr} above which reversible magnetic behaviour is observed in the torque experiments. Also shown (black) are data points corresponding to the flux-lattice line measured by Taylor and Maple on different samples with similar nominal doping[34]. The temperature dependent values of H_{irr} for all samples from a single source can be fit to the Lindemann model for $T_c = 57.5$ K and $\mu_0 H_{c2} = 60 \pm 5$T.

Estimation of the electronic heat capacity

The measured heat capacity ($\gamma_N T$) at temperatures marginally above T_c provides an estimate of the normal contribution to the electronic coefficient of heat capacity $\gamma_C T$, which is expected to decrease with decreasing T in the pseudogap regime. Measurements in ref. 37 on samples similar in composition to those measured in the current study yield a value of $\gamma_N \approx 10$ mJmol^{-1}K^{-2}. Further, experiments performed in fields of up to 13 T [ref. 38] find no magnetic field dependence of γ_N within the resolution of the measurement.

In the case of the quantum oscillation experiments, the Q2D electronic structure of $YBa_2Cu_3O_{6.51}$ implies that only the magnitude of the effective mass of the carriers in each individual pocket is relevant for estimating its contribution to the electronic heat capacity.[8] On assuming a Kramers degeneracy, each pocket contributes $|m^*/m_e| \times 1.46$ mJmol^{-1}K^{-2} to γ_m, irrespective of the carrier type.

Fermi surface reconstruction for ordering wavevectors away from Q = (π,π)

The unreconstructed Fermi surfaces in Figs. 4a and c are calculated using a t,t',t'' tight binding parameterisation of the dispersion $\varepsilon_{\mathbf{k}}$ (refs. 13, 39) with t = 380 meV, t'/t = -0.32 and t''/t = 0.16. For schematic purposes, a value of $\Delta_1 \sim 0.83t$ is used in calculating the reconstructed bands (shown in Fig. 4d) to lowest order using $\varepsilon^{\pm}_{\mathbf{k}} = \frac{1}{2}\left(\varepsilon_{\mathbf{k}} + \varepsilon_{\mathbf{k+Q}}\right) \pm \sqrt{\frac{1}{4}\left(\varepsilon_{\mathbf{k}} - \varepsilon_{\mathbf{k+Q}}\right)^2 + \Delta_1^2}$, where '+' denotes the upper electron band and '-' denotes the lower hole band. Hole pockets appear for all non-zero Δ_1/t provided the system is hole doped ($p > 0$), whereas the existence of electron pockets requires that $\Delta_1/t \leq 1$ for $p_{\mathrm{nom}} = 0.1$. On adopting an alternative parameterisation scheme with t'/t = -0.34 and t''/t = 0 corresponding to a simple circular unreconstructed Fermi surface, the experimentally observed pockets can be similarly reproduced on using a smaller value of $\Delta_1 \sim 0.33t$ and similar value of δ.

In the case of an helical or spiral spin-density wave where $\mathbf{Q} \neq (\pi,\pi)$, the scattering potential introduced by $\mathbf{S}(\mathbf{R}) = \cos(\mathbf{Q}\bullet\mathbf{R})S_x + \sin(\mathbf{Q}\bullet\mathbf{R})S_y$ couples down-spin electrons at wavevector **k** to up-spin electrons at **k** + **Q** and up-spin electrons at **k** to down-spin electrons at **k** – **Q**, or vice versa. For simplicity, only the couplings between **k** and **k** + **Q** are shown in Fig. 4d. Including both in the extended Brillouin zone representation yields a Fermi surface of the form shown in Fig. S4a whereas considering only couplings between **k** and **k** + **Q** in the repeated Brillouin zone representation yields a Fermi surface of the form shown in Fig. S4b.

In the case of a collinear spin-density wave where $\mathbf{Q} \neq (\pi,\pi)$, the scattering potential introduced by $\mathbf{S}(\mathbf{R}) = \cos(\mathbf{Q}\bullet\mathbf{R})S_z$ couples electrons at wavevector **k** to those of the same spin at both **k** + **Q** and **k** – **Q**, opening twice as many gaps compared to the helical or spiral scenario. In general, collinear order leads to a hierarchy of gaps coupling different orders of ± n**Q** [ref. 40]. If one considers the additional gaps to occur wherever the repeated translations by **Q** in Fig. S4**b** intersect, for example, this will lead to open Fermi surface sheets with small or no hole pockets, as recently shown by Millis and Norman[13]. Larger hole orbits may, however, arise in sufficiently strong magnetic fields due to magnetic breakdown tunnelling overcoming the gaps, as has been experimentally shown in the case of the well known incommensurate spin-density wave system Cr (ref. 41) .

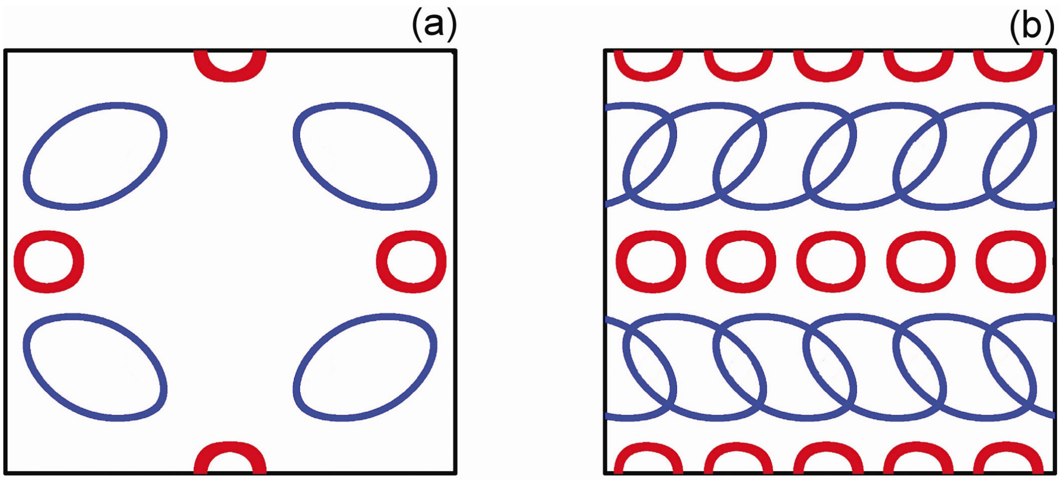

Fig. S4. Reconstructed Fermi surfaces. (a) shows that of a helical or spiral spin-density wave in the extended Brillouin zone representation including couplings between **k** and both **k** + **Q** and **k** - **Q**, whereas (b) shows only couplings between **k** and **k** + **Q** in the repeated zone representation.

Additional experimental results

In addition to torque experiments on $YBa_2Cu_3O_{6.51}$, similar experiments are performed on a crystal of $YBa_2Cu_3O_{6.50}$, yielding dHvA oscillations of both the α and β frequencies (see Fig. S5). Shubnikov-de Haas (SdH) experiments are also performed on the $YBa_2Cu_3O_{6.51}$ crystal in a motor-generator-driven magnet to ~ 55 T (in Los Alamos) using a contactless technique (results shown in fig. S6). The sample is placed inside an 8 turn compensated coil that forms part of a ~46 MHz tunnel diode oscillator (TDO) circuit. The resistive state induced on suppressing superconductivity by a magnetic field[7] enables the oscillatory ~10^{-7} T electromagnetic field of the TDO to penetrate ~ 100 μm into the sample. The resulting shift in the TDO frequency is linearly related to the orbitally-averaged in-plane resistivity $(\rho_{xx} + \rho_{yy})/2$. TDO measurements are performed in a ^{3}He refrigerator with the sample GE-varnished to a sapphire plate (to minimise sample heating), both of which are in direct contact with liquid ^{3}He below ~ 2K and ^{3}He gas at higher temperatures. Over the regime where vortex motion dissipation dominates ($\mu_0 H \leq 30$ T) the magnetic field of the motor-generator magnet is swept at a slow rate of ~20 Ts $^{-1}$ – a sweep rate which is still ~100 times that employed in the DC field torque experiments described in this work. In the case of high T_c experiments in non-DC magnetic fields, a rise in sample temperature is inevitable due to considerable heat generated from flux-flow dissipation in the vortex state in response to a rapidly varying magnetic field. Despite this limitation, the slow sweep rate in the motor-generator magnet and the good thermal contact of the sample immersed in liquid ^{3}He enables a lowest sample temperature of ~1 K to be accessed when the ^{3}He refrigerator is cooled to 0.3 K.

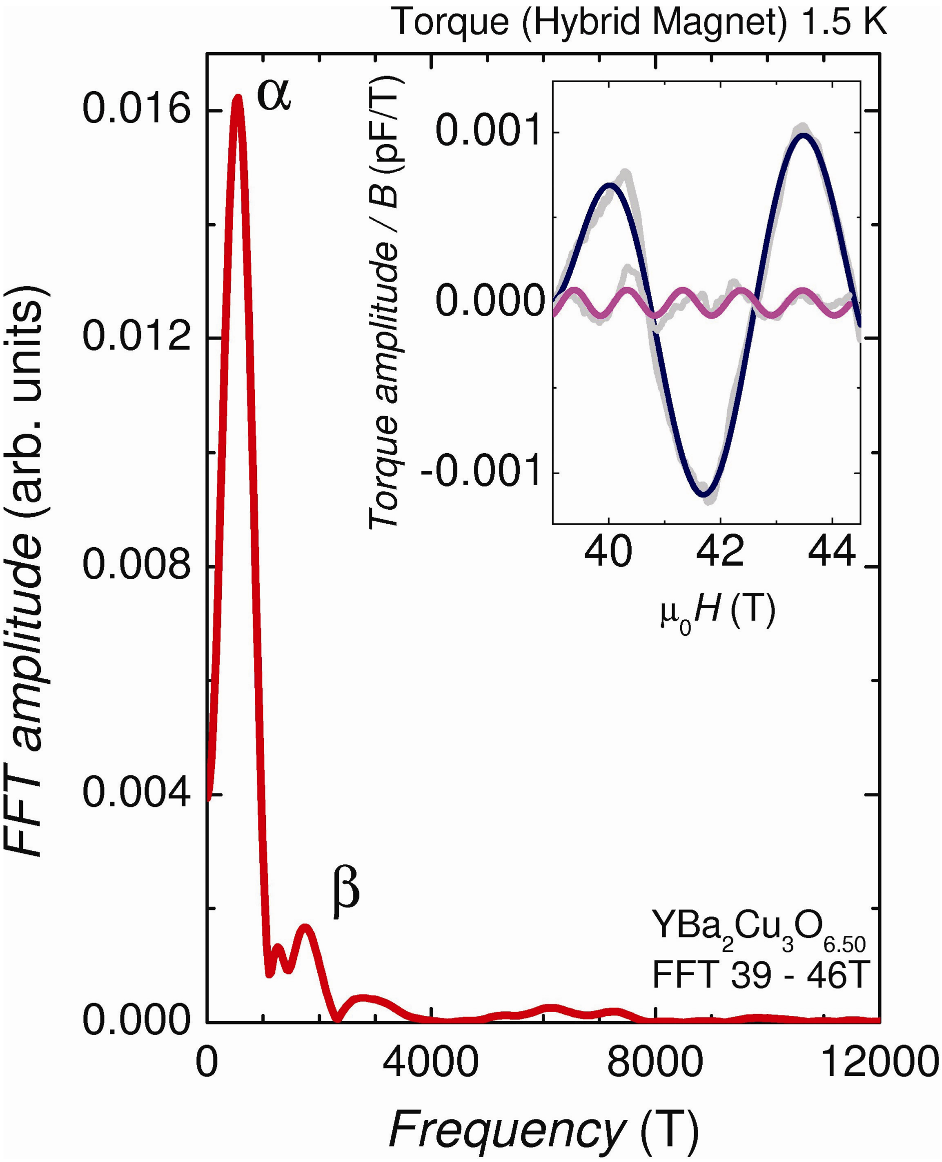

Fig. S5. de Haas-van Alphen effect in $YBa_2Cu_3O_{6.50}$. Fourier transform of 17 up and down averaged magnetic field sweeps showing the α and β frequencies ($F_\alpha = 490 \pm 30$ T and $F_\beta = 1700 \pm 50$ T). The inset shows the dHvA oscillations together with those of just the β frequency after fitting and subtracting the α frequency and polynomial component as for $YBa_2Cu_3O_{6.51}$. Fits to the oscillations are shown as guides to the eye.

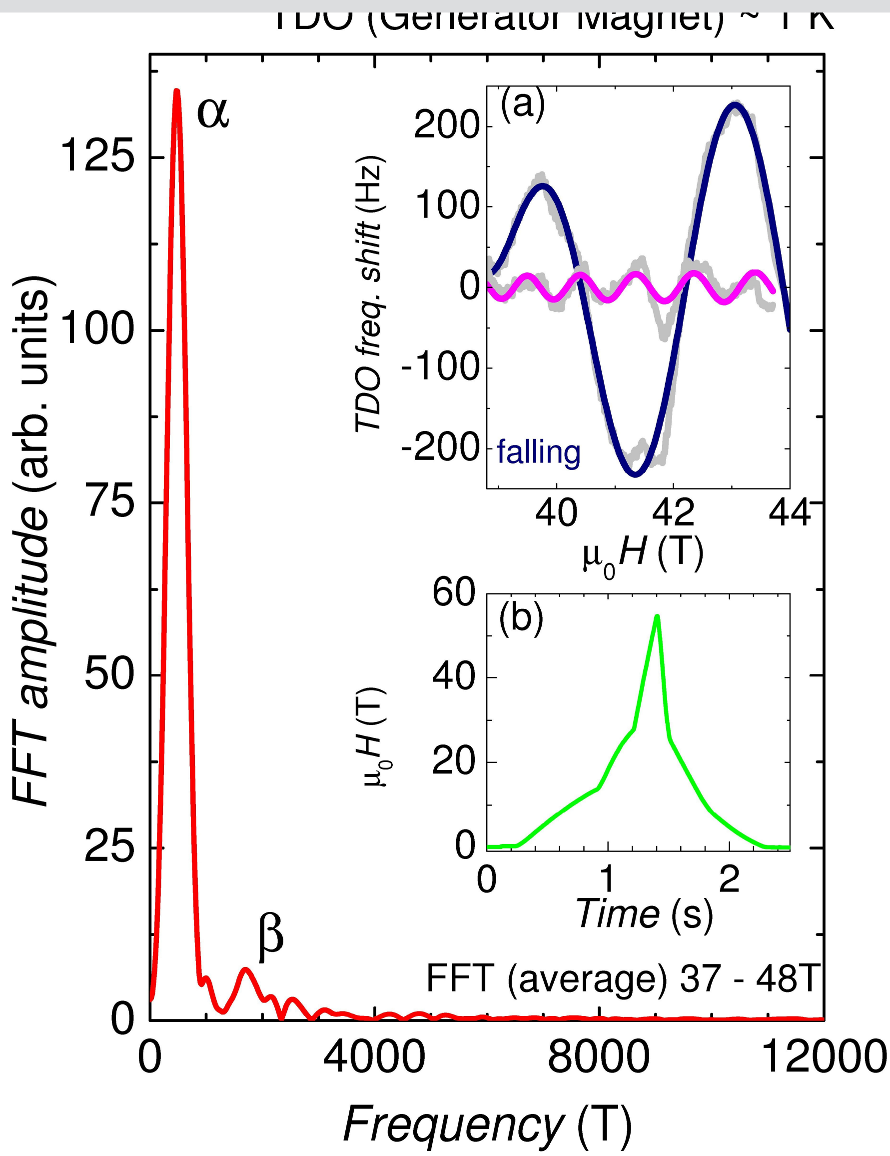

Fig. S6. Shubnikov-de Haas effect in $YBa_2Cu_3O_{6.51}$. Fourier transform of oscillations averaged over 4 rising and falling sweeps in a field range 37 to 48 T comparable to the magnetic torque study (where the β appears most prominently in the SdH signal). Frequencies F_α = 510 ± 20 T and F_β = 1640 ± 50 T are measured, consistent with both the α and β frequencies in Fig. 2 of the main manuscript. Oscillations over a wider field range may indicate preliminary evidence for a slower frequency 250 ± 100 T, possibly consistent with the presence of a γ pocket[42]. Inset (a) shows the SdH oscillations together with the isolated β frequency after fitting and subtracting the α frequency and polynomial components as described in the main manuscript. Inset (b) shows the shape of the magnetic field sweep in the generator magnet, which has a relatively slow ramp rate ~ 20Ts^{-1} in the vortex state up to ~20T.

References

33. Harrison, N. *et al*. Numerical model of quantum oscillations in quasi-two-dimensional organic metals in high magnetic fields. *Phys. Rev. B* **54**, 9977-87 (1996).

34. Taylor, B. J., and Maple, M. B. Evolution and analysis of the vortex liquid melting line in $Y_{1-x}Pr_xBa_2Cu_3O_{6.97}$ and $YBa_2Cu_3O_{6.5}$. *Phys. Rev. B* **76**, 014517 (2007).

35. Miller, P. & Györffy, B. L. Theoretical investigations of the vortex lattice and de Haas-van Alphen oscillations in the superconducting state. *J. Phys.: Condens. Matter* **7**, 5579-5606 (1995).

36. Yasui, K. & Kita, T. Theory of the de Haas-van Alphen effect in type-II superconductors. *Phys. Rev. B* **66**, 184516 (2002).

37. Loram, J. W. *et al*. Electronic specific heat of $YBa_2Cu_3O_{6+x}$ from 1.8 K to 300 K. *Phys. Rev. Lett.* **71**, 1740-1743 (1993).

38. Luo, J. L., Loram, J. W., Cooper, J. R., Mirza, K. A. & Jin, D. Specific heat of $Y_{0.8}Ca_{0.2}Ba_2Cu_3O_{7-\delta}$. *Physics B* **284-288**, 1045-1046 (2000).

39. Andersen, O. K. et al. LDA energy bands, low-energy Hamiltonians, t', t'', $t_\perp(\mathbf{k})$, and $J_\perp$. J. Phys. Chem. Solids **56**, 1573-1591 (1995).

40. Lomer, W. M. *Electron orbits in antiferromagnetic chromium*. (Proceedings of the International Conference on Magnetism, Nottingham, UK, 1964).

41. Reifenberger, R., Holroyd, F. W. & Fawcett, E. Electron interference oscillations and spin-density-wave energy gaps at the Fermi surface of antiferromagnetic chromium. *J. Low Temp. Phys*. **38**, 421-445 (1980).

42. We acknowledge informative discussions with S. Chakravarty in this regard.